

Electrochemical Synthesis of Mesoporous Architected Ru Films Using Supramolecular Templates

Kenya Kani, Joel Henzie, Ömer Dag, Kathleen Wood, Muhammad Iqbal, Hyunsoo Lim, Bo Jiang, Carlos Salomon, Alan E. Rowan, Md. Shahriar A. Hossain, Jongbeom Na,* and Yusuke Yamauchi*

The electrochemical synthesis of mesoporous ruthenium (Ru) films using sacrificial self-assembled block polymer micelles templates, and its electrochemical surface oxidation to RuO_x is described. Unlike standard methods such as thermal oxidation, the electrochemical oxidation method described here retains the mesoporous structure. Ru oxide materials serve as high-performance supercapacitor electrodes due to their excellent pseudocapacitive behavior. The mesoporous architected film shows superior specific capacitance ($467 \text{ F g}^{-1}_{\text{Ru}}$) versus a nonporous Ru/ RuO_x electrode ($28 \text{ F g}^{-1}_{\text{Ru}}$) that is prepared via the same method but omitting the pore-directing polymer. Ultrahigh surface area materials will play an essential role in increasing the capacitance of this class of energy storage devices because the pseudocapacitive redox reaction occurs on the surface of electrodes.

conductivity, an abundance of active catalytic sites, and good mass transport due to the porous structure. Additionally, porous architecture can also provide unique active sites such as atomic kinks and steps which can further improve the inherent catalytic performance toward various electrochemical reactions such as fuel cells,^[1,2] water-splitting devices,^[3,4] and sensors.^[5,6] In the past decade, various methods have been developed to synthesize mesoporous metals, including hard-templating and soft-templating methods. While hard-templates offer a reliable and intuitive approach to generate mesoporous metals, the complexity of the technique, the lack of morphology control, and the use of

1. Introduction

Mesoporous metal nanoarchitectures have attracted a lot of interest as electrocatalysts due to their excellent electrical

harsh chemicals have limited their impact in broader applications.^[7–9] Soft-templating methods using molecular templates such as lyotropic liquid crystals (LLCs) and micelle assemblies were developed to solve some of the limitations of hard


K. Kani, H. Lim, Prof. A. E. Rowan, Dr. Md. S. A. Hossain, Dr. J. Na, Prof. Y. Yamauchi
Australian Institute for Bioengineering and Nanotechnology (AIBN)
The University of Queensland
Brisbane, QLD 4072, Australia
E-mail: j.na@uq.edu.au; y.yamauchi@uq.edu.au

Dr. J. Henzie, Dr. M. Iqbal, Dr. B. Jiang, Dr. J. Na, Prof. Y. Yamauchi
International Center for Materials Nanoarchitectonics (WPI-MANA)
National Institute for Materials Science (NIMS)
1-1 Namiki, Tsukuba, Ibaraki 305-0044, Japan

Prof. Ö. Dag
Department of Chemistry and UNAM-National Nanotechnology
Research Center
Bilkent University
Ankara 06800, Turkey

Dr. K. Wood
Australian Nuclear Science and Technology Organisation (ANSTO)
New Illawara Rd, Lucas Heights, NSW 2234, Australia

Dr. C. Salomon
Exosome Biology Laboratory
Centre for Clinical Diagnostics
The University of Queensland Centre for Clinical Research
Royal Brisbane and Women's Hospital
The University of Queensland
Brisbane, QLD 4029, Australia

 The ORCID identification number(s) for the author(s) of this article can be found under <https://doi.org/10.1002/smll.202002489>.

Dr. C. Salomon
Department of Clinical Biochemistry and Immunology
Faculty of Pharmacy
University of Concepción
Concepción 4030000, Chile

Dr. Md. S. A. Hossain
School of Mechanical and Mining Engineering
Faculty of Engineering
Architecture and Information Technology (EAIT)
The University of Queensland
Brisbane, QLD 4072, Australia

Prof. Y. Yamauchi
School of Chemical Engineering
Faculty of Engineering
Architecture and Information Technology (EAIT)
The University of Queensland
Brisbane, QLD 4072, Australia

Prof. Y. Yamauchi
Department of Plant and Environmental New Resources
Kyung Hee University
1732 Deogyong-daeo, Giheung-gu, Yongin-si
Gyeonggi-do 446-701, South Korea

DOI: 10.1002/smll.202002489

templates for the development of mesoporous metals.^[10–15] In particular, soft-templating methods that use surfactants and low-molecular-weight block copolymers have proven to be a versatile route to mesoporous/dendritic metals with small pore diameters (<10 nm).^[16–18] However, it is desirable to generate mesoporous metals with even larger pores to enable better mass transport properties and enhance the accessibility of active catalytic sites. Our previous work described the utilization of high-molecular-weight block copolymer micelles as pore-directing agents to fabricate metallic films perforated with mesopores, as well as mesoporous nanoparticles with tunable pore sizes. These porous network materials supported high (electro)catalytic activities in various reactions.^[1–3,6,19–25]

Ruthenium oxide (RuO₂)-based materials support high specific capacitances in aqueous supercapacitor (pseudocapacitor) devices ranging from several hundreds to ≈1000 F g^{−1}.^[26] They function via fast, highly reversible surface redox reactions. Thus, control of crystallinity, hydration, and surface area are critical variables in improving charge storage.^[27–29] High-capacitance RuO₂ materials have been traditionally synthesized either by hydrothermal synthesis in one step or by sol-gel synthesis followed by thermal annealing.^[28,30–32] Controlling the latter annealing process is challenging because water may be driven from the structure during material transformation, resulting in a loss of capacitance. For example, it was reported that RuO_x annealed at 400 °C generated RuO₂·0.03H₂O with a specific capacitance of only 29 F g^{−1}, whereas RuO_x annealed at 150 °C generated RuO₂·0.5H₂O with a specific capacitance of ≈900 F g^{−1}.^[33] High temperatures also tend to collapse the mesoporous network which limits capacitance. Therefore, we have been searching for a variation on the soft-templating approach using electrodeposition to generate robust porous networked films, while maintaining a relatively high concentration of water in the final structure.

Here, we report the first example of an electrochemical process to generate extended mesoporous Ru films (MRFs) with large pores and uniform overlapping networks of channels for good mass transport in electrochemical reactions. We used block copolymer micelle templates as pore-directing agents and sacrificial templates to generate the mesoporous metal. By tuning the applied potentials, it is possible to control electrodeposition of the Ru metal on the conductive substrate, enabling the electrodes to be used immediately as electrodes. The Ru metal is subsequently oxidized electrochemically to RuO_x for use as a supercapacitor electrode. Unlike other porous RuO_x generated by either thermal oxidation or hydrothermal synthesis, electrochemical oxidation is gentler and does not destroy the porous network because only the top surface on the pore walls is oxidized.

2. Result and Discussion

As described in the Experimental Section, MRFs are produced via electrochemical deposition using self-assembled polymeric micelles as soft templates (Figure S1, Supporting Information). The scanning electron microscopy (SEM) images (Figure 1a,b) of as-prepared MRF show the presence of numerous pores on the top surface. The pores were uniform across a large area

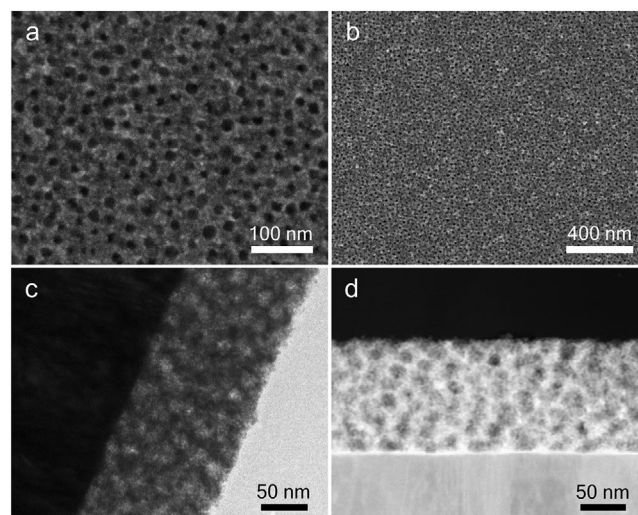


Figure 1. a,b) The top-surface SEM images with different magnifications, c) cross-sectional TEM, and d) HAADF-STEM images of MRF deposited at −0.6 V for 1200 s.

of the film without significant defects. The SEM images were used to measure the diameters of >200 pores and pore walls, giving an average pore diameter of 13.2 nm and wall thickness of 11.4 nm (Figure S2, Supporting Information). The MRF was ≈100 nm thick after 1200 s deposition, indicating an average growth rate of 0.08 nm s^{−1}. Deposition experiments performed at various applied deposition times show the orthogonal growth of the film is linear; thus film thickness can be controlled by simply modifying the deposition time (Figure S3, Supporting Information). Transmission electron microscopy (TEM) observations (Figure 1c) indicate that there are numerous pores dispersed throughout the film, and the presence of porous structure is more apparent in the high-angle annular dark-field scanning TEM (HAADF-STEM) image (Figure 1d). On the other hand, nonporous Ru film (NRF) prepared in the absence of polymeric micelles does not possess such a uniform mesoporous structure, proving that the micelles act as a pore-directing agent (Figure S4, Supporting Information).

Micelle formation in the solution can be visualized using the Tyndall effect (Figure S1, Supporting Information), but the presence of micelles was further confirmed by staining them with a 1% phosphotungstic acid (PTA) solution where pH was adjusted to 7 with sodium hydroxide (NaOH) solution (Figure 2a,b). The white areas in the TEM images correspond to the core of micelles (poly(methyl methacrylate) (PMMA)) since PTA primarily localizes in the hydrophilic poly(ethylene oxide) (PEO) shell. The average diameter of micelle prepared in the absence of Ru precursors was 15.2 nm, which is slightly smaller than micelles decorated with Ru precursors (17.4 nm) (Figure S5, Supporting Information). The micelles were round in both experiments, demonstrating that the micelles are not affected by the Ru precursors. Furthermore, small-angle neutron scattering (SANS) measurements were performed using the Bilby instrument^[34] to investigate the micelles in solution (Figure 2c,d) and data reduced using standard procedures.^[35] The radii of gyration of the scattering particles were extracted from the linear Guinier region at low *q* (Figure 2c) using

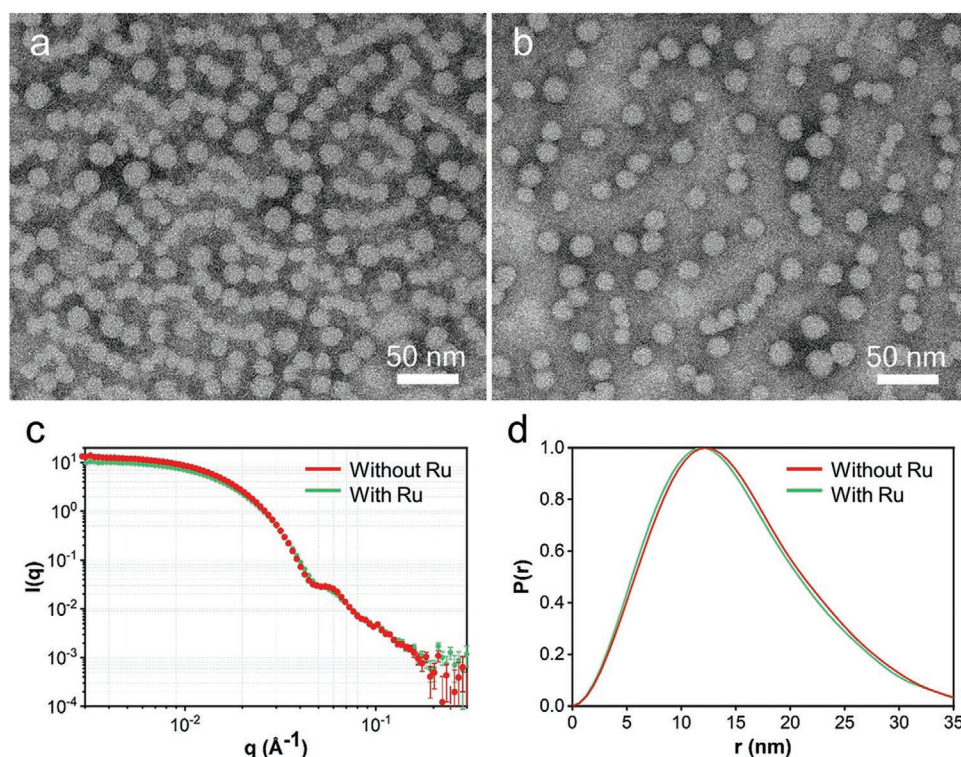


Figure 2. TEM observations of polymeric micelles prepared by mixing a) PEO-*b*-PMMA, THF, and water, b) PEO-*b*-PMMA, THF, $\text{RuCl}_3(\text{aq})$, and water. c) SANS patterns and d) radial probability distribution function extracted from SANS data of the corresponding samples.

Primus^[36] and found to be 11.4 and 11.5 nm for the solutions without and with Ru precursors, respectively. These values are in good agreement with the real space radii of gyration obtained from probability distribution functions (11.4 and 11.6 nm, respectively) in Figure 2d. Unlike the TEM observation, the SANS patterns contain information on the scattering properties of the whole micelle, including both PEO and PMMA units. Therefore, the micelle diameters obtained from SANS measurement (≈ 23 nm) are larger than the values found in the TEM observations, since vacuum condition in TEM also can cause micelle shrinkage. Considering the TEM and SANS data, the micelles are spherical and appear to be stable enough to transfer this shape into the porous metal electrode.

The interaction between the micelles and Ru precursors can be studied qualitatively using ultraviolet–visible spectroscopy (UV–vis) (Figure 3). We examined four different solutions: (A) the typical reaction solution (B) without water, (C) without polymer, and (D) without Ru(III) chloride (RuCl_3). Solution D does not have any absorbance peaks. Thus, the peaks observed in the other solutions come from the Ru species. RuCl_3 dissolves in various media to form several equilibrium species such as $[\text{RuCl}_n(\text{H}_2\text{O})_{(6-n)}]^{(3-n)+}$, where n varies from 6 to 0, resulting in $[\text{RuCl}_6]^{3-}$, $[\text{RuCl}_5(\text{H}_2\text{O})]^{2-}$, $[\text{RuCl}_4(\text{H}_2\text{O})_2]^{-}$, $[\text{RuCl}_3(\text{H}_2\text{O})_3]$, $[\text{RuCl}_2(\text{H}_2\text{O})_4]^+$, $[\text{RuCl}(\text{H}_2\text{O})_5]^{2+}$, and $[\text{Ru}(\text{H}_2\text{O})_6]^{3+}$ species in our reaction solution. Since our reaction solution is aqueous, the water coordinated species (i.e., $[\text{RuCl}_3(\text{H}_2\text{O})_3]$, $[\text{RuCl}_2(\text{H}_2\text{O})_4]^+$, $[\text{RuCl}(\text{H}_2\text{O})_5]^{2+}$, and $[\text{Ru}(\text{H}_2\text{O})_6]^{3+}$) dominate. Whereas acidic aqueous solutions tend to generate $[\text{RuCl}_2(\text{H}_2\text{O})_4]^+$, $[\text{RuCl}(\text{H}_2\text{O})_5]^{2+}$, and $[\text{Ru}(\text{H}_2\text{O})_6]^{3+}$ ion species.^[37,38] Increasing the number of water in the coordination sphere of Ru blueshifts

the d-d transitions of Ru(III) in the UV–vis spectra. The features with high extinction coefficients ($11\,300\text{--}15\,000\text{ cm}^{-1}\text{ M}^{-1}$) at ≈ 300 and 400 nm in A, B, and C are caused by ligand-to-metal charge transfer (LMCT). In solution B these bands are redshifted, indicating that the Cl^- coordination is favored in tetrahydrofuran (THF), resulting in negatively charged complexes. Positively charged aqua complexes are favored in water. Comparing spectra A and C, the addition of polymer to the solution does not alter the chemical nature of the complexes as expected. As shown in spectrum B, all the peaks derived from d-d and LMCT transitions are redshifted, suggesting the

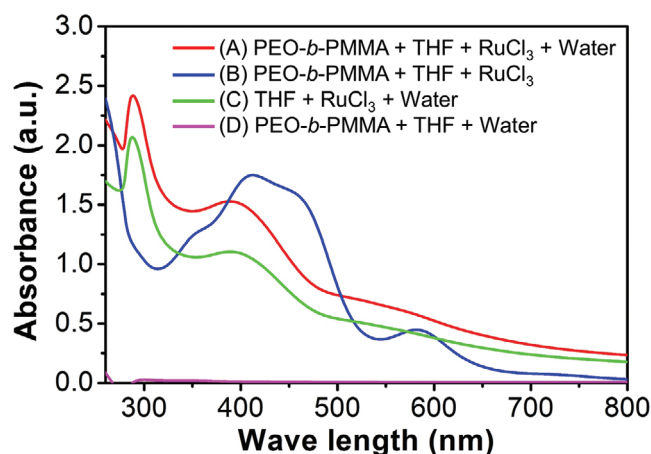


Figure 3. UV–vis absorption spectra of various solutions described in the figure legend.

presence of Cl^- rich coordination around Ru(III) without water. Additional peaks (e.g., shoulder tailing from 500 to 600 nm in aqueous media and around 720 nm in THF) may be due to d-d transitions ($^2T_{2g}$ ground state to $^2A_{2g}/^2T_{1g}$ or 2E_g excited states). The blueshift from 720 to 550 nm is consistent with the above interpretation, since chloride is a π -donor ligand. Overall, these results suggest that water media favors the positively charged water-rich complexes. The PEO interacts with water via hydrogen bonding, which helps concentrate Ru(III) species around the PEO micelle shells.^[39] The Ru complexes impart a collective positive charge on the micelles and enable the supra-molecular template to be electrodeposited on the surface of the cathode and subsequently reduced from Ru(III) to Ru(0) metal to generate the MRF.

Wide-angle X-ray diffraction (XRD) was used to study the crystallinity and metallic nature of the MRF (Figure S6a, Supporting Information). The pattern matches with the hexagonal closest packed (hcp) structure of Ru, with six distinct peaks at 38.4° (100), 44.0° (101), 58.3° (102), 69.4° (110), 78.4° (103), and 84.7° (112), corresponding to 2θ (Miller indices). The electron diffraction pattern illustrates the polycrystalline feature with the concentric rings of spots, and that match the Ru hcp crystal structure (Figure S6b, Supporting Information). Using the (101) peak in XRD, the average domain size was 3.9 nm, according to the Scherrer equation (shape factor = 0.9). It is smaller than the thickness of the pore walls, indicating that the pore walls are constructed of tiny nanoparticles, which matches our high-resolution TEM (HRTEM) images (Figure S6c, Supporting Information). The combination of the mesopores and the interparticle space created from these small nanoparticles may maximize the surface area of the electrode and enhance the diffusion of reactants. We examined the top edge of the MRF with HRTEM and observed the Ru lattice in addition to unsaturated Ru atoms at kinks and steps on the surface of the electrode (Figure S6d, Supporting Information).

Linear sweep voltammetry (LSV) was used to investigate the effect of applied potential on Ru deposition in order to discover the optimal conditions for MRF formation. The measurements were performed in the reaction solution using an applied potential between -0.2 to -1.0 V (vs Ag/AgCl) with a scan rate of 50 mV s^{-1} (Figure S7a, Supporting Information). According to the obtained curve, the deposition of Ru ($\text{Ru}^{3+} + 3\text{e}^- \rightarrow \text{Ru}$) begins at around -0.5 V. To examine the influence of potential, we performed deposition experiments at five different potentials spanning -0.5 to -0.9 V using a constant deposition time ($t = 1200$ s). SEM images show that more negative potentials do not produce a uniform porous structure, due to a combination of hydrogen generation and reaction kinetic that is too fast to incorporate the micelles in the film (Figure S7b–f, Supporting Information). Although the MRFs prepared at -0.5 and -0.6 V possess similar structure, the growth rate is slower at -0.5 V and the thickness is not enough to cover the substrate (inset images in Figure S7b,c, Supporting Information). Therefore, we employed -0.6 V as the optimal deposition potential, and all the samples are prepared at this potential for further electrochemical measurements. The detailed discussion on the current efficiency is shown in Figure S8 (Supporting Information).

Electrochemically active surface areas (ECSAs) were measured via copper underpotential deposition (Cu upd) stripping

as described in the Experimental Section. (More details about polarization potential and time are discussed in Figure S9 (Supporting Information).) According to the integrated areas of Cu upd stripping peaks (Figure S10a,b, Supporting Information), ECSA of the MRF prepared at -0.6 V for 1200 s was $48.5 \text{ m}^2 \text{ g}^{-1}$, which is much higher than the NRF ($9.8 \text{ m}^2 \text{ g}^{-1}$) sample prepared without micelles. Moreover, the ECSA increased proportionally against the film thickness (i.e., deposition time). This is a significant trend, suggesting that all pores found in our MRF are accessible and electrochemically active even when the film becomes thicker (Figure S10c, Supporting Information). When ECSAs are normalized by volume, relatively constant values are found over different deposition times (Figure S10d, Supporting Information), which also indicates the homogeneous pore distribution even for thicker films.

For the application as a supercapacitor electrode, the as-prepared MRF was modified to mesoporous Ru/RuO_x (Meso-Ru/RuO_x), where RuO_x is the surface oxidized by an electrochemical oxidation process. Compared to other noble metals such as platinum (Pt), rhodium (Rh), palladium (Pd), and gold (Au), Ru electrode has much more hysteresis between the anodic and cathodic polarization in the typical cyclic voltammetry (CV) range. This is because the reduction of surface oxide is much slower than its formation in the anodic scan and never recovers to the original metallic surface, especially when the potential is swept to >0.8 V (vs reversible hydrogen electrode (RHE)).^[40,41] Hence, by intentionally running many CVs at higher potentials, the surface of Ru electrodes is gradually covered by an oxide layer. In our experiment, we perform 500 cycles CV from 0.2 to 1.2 V (vs RHE) at the scan rate of 50 mV s^{-1} in 0.5 M sulfuric acid (H_2SO_4) solution (Figure 4a). The fast scan rate and cutting the hydrogen region (0 – 0.2 V vs RHE) can minimize the time for the oxide layer to be formed, leading to an efficient surface oxidation process. The oxide formation peak at ≈ 1.2 V vanishes with repeating the potential sweeps, indicating that there are no metallic Ru sites to be oxidized on the surface after 500 cycles (i.e., all surfaces are covered by oxide layer). In addition, new reversible redox feature emerges at ≈ 0.7 V, which matches the conversion between Ru(IV) and Ru(III). As shown in Figure 4b, the Cu upd behavior is not observed on the as-processed Meso-Ru/RuO_x electrode, while the apparent Cu upd stripping peak can be found on the MRF before oxidation (Figure S10a, Supporting Information). This is also good evidence of the formation of surface oxide since the Cu does not deposit on the oxide surface.^[41] To further prove the presence of the surface oxide layer, X-ray photoelectron spectroscopy (XPS) spectra were analyzed for the MRF and NRF (Figure 4c,d). Before oxidation, the binding energies (BEs) of the Ru $3p_{3/2}$ peaks are located at 461.3 (MRF) and 461.5 eV (NRF), matching the reported values for a metallic Ru⁰ surface that is partially oxidized in air. Upon electrochemical oxidation, the BEs of Ru $3p_{3/2}$ peaks shift to 462.8 (Meso-Ru/RuO_x) and 462.5 eV (nonporous Ru/RuO_x; NP-Ru/RuO_x), respectively, and they match Ru⁴⁺ electronic state, proving that the surface is completely oxidized. The slightly higher BE peak of Meso-Ru/RuO_x may indicate the formation of hydrated species.^[42] Interestingly, wide-angle XRD patterns (Figure S11, Supporting Information) of Meso-Ru/RuO_x and NP-Ru/RuO_x samples indicate that the bulk of the film is not changed significantly by electrochemical oxidation, suggesting

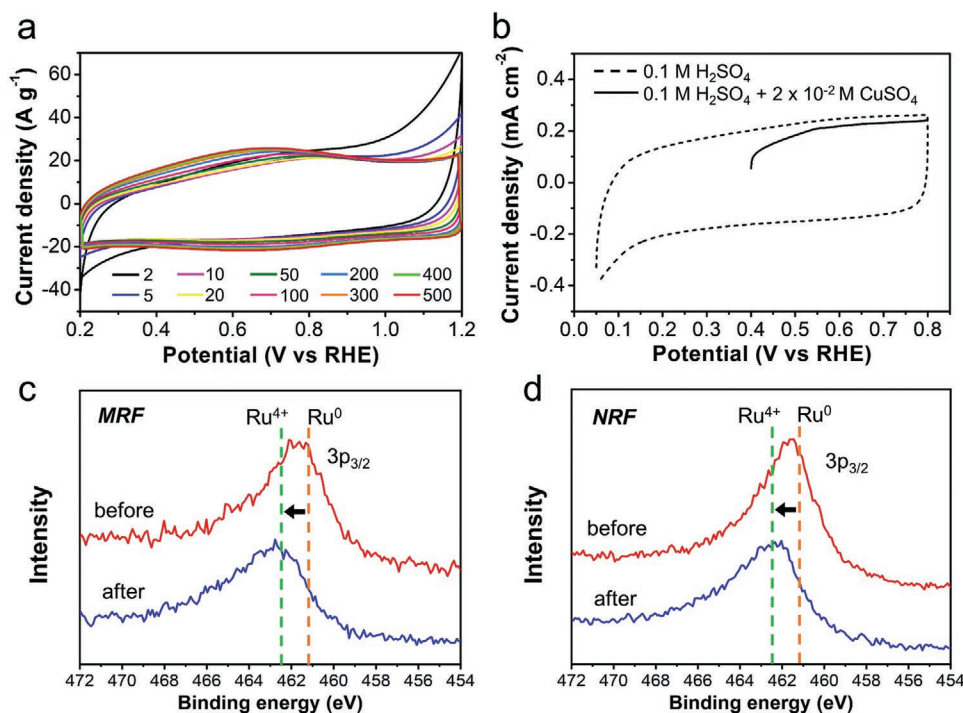


Figure 4. a) 500 cycles CV of MRF obtained during electrochemical surface oxidation in 0.5 M H_2SO_4 at the scan rate of 50 mV s^{-1} . b) CV (dash) and LSV (solid) curves of Meso-Ru/ RuO_x obtained in 0.1 M H_2SO_4 and 0.1 M $\text{H}_2\text{SO}_4 + 2 \times 10^{-2} \text{ M CuSO}_4$, respectively. c, d) Ru $3p_{3/2}$ XPS spectra of MRF and NRF before and after the oxidation process.

that only the top few layers of exposed pore walls are oxidized. The crystal structure as well as porous architecture are not destroyed (The data are given in the later section.).

Finally, we checked the performance of the Meso-Ru/ RuO_x and NP-Ru/ RuO_x deposited at -0.6 V for 1200 s as supercapacitor electrodes (Figure 5 and S12, Supporting Information). The capacitance value of Meso-Ru/ RuO_x obtained from CV at the scan rate of 1 mV s^{-1} is calculated to be $467 \text{ F g}^{-1}_{\text{Ru}}$, and matches the value obtained with galvanostatic charge/discharge (GCD) measurements at a current density of $0.5 \text{ A g}^{-1}_{\text{Ru}}$. Moreover, the capacitance is retained very well even when a faster charge/discharge process (i.e., larger current density) is applied, indicating fast ion transport. The CV curves are not rectangular at higher scan rates, while they show a typical rectangular shape at lower scan rates. Therefore, we may need to prepare mesoporous films with larger pores to improve the accessibility of reactants and achieve more effective performance. Overall, the Meso-Ru/ RuO_x has a specific capacitance 17 times higher than the NP-Ru/ RuO_x ($467 \text{ vs } 28 \text{ F g}^{-1}_{\text{Ru}}$), while its ECSA is only five times larger (Figure 5b). Even when the capacitance is normalized by ECSA, the Meso-Ru/ RuO_x ($0.96 \text{ mF cm}^{-2}_{\text{ECSA}}$) has 3.3 times higher performance than NP-Ru/ RuO_x ($0.29 \text{ mF cm}^{-2}_{\text{ECSA}}$). These results indicate that the mesoporous architecture not only enhances the surface area but also imparts other favorable properties toward specific capacitance. One possible cause of enhanced performance might be the presence of hydrated surface species, which are indicated by XPS. And it has been reported that hydrous regions promote proton permeation into the structure and allow efficient charge storage along with the excellent electron conductivity derived from both

metallic Ru framework and RuO_x surface.^[27–29] Furthermore, the fact that NRF has only tiny spaces in the bulk-like structure (Figure S4, Supporting Information) might contribute to poor capacitance since these small pores may collapse during the oxidation process, resulting in a loss of surface area. Finally, long-term stability tests were conducted by running a 2000 cycles charge/discharge process at the current density of $10 \text{ A g}^{-1}_{\text{Ru}}$ (Figure 5e). The as-prepared Meso-Ru/ RuO_x shows excellent stability and even activated after several cycles. (Capacitance retention ends up with 111% after 2000 cycles.) Furthermore, the SEM observation of used sample confirms that the porous structure is not affected by both the oxidation process and the stability test (Figure 5f).

To date, several efforts have been made to prepare mesoporous RuO_x materials by templating methods. However, in most cases, the resulting porous structure is not uniform due to harsh chemical conditions and highly viscous solutions. Although some of these previous works reported ordered porous structures, their pore size is limited to $<10 \text{ nm}$ in diameter. Our method solves many of the challenges in this work because polymer micelles are quite rugged in electrochemical deposition processes. Moreover, it is also possible to fabricate patterned substrates by modifying the surface conductivity of the substrates.^[43] Since Ru is a precious metal and not abundant, the usage should be restricted to small-area applications such as microdevice supercapacitors, which is desirable for our modern society demanding various portable devices. However, traditional powder-state supercapacitor materials are quite difficult to be loaded on such microscale devices, and preparing mesoporous materials on the patterning

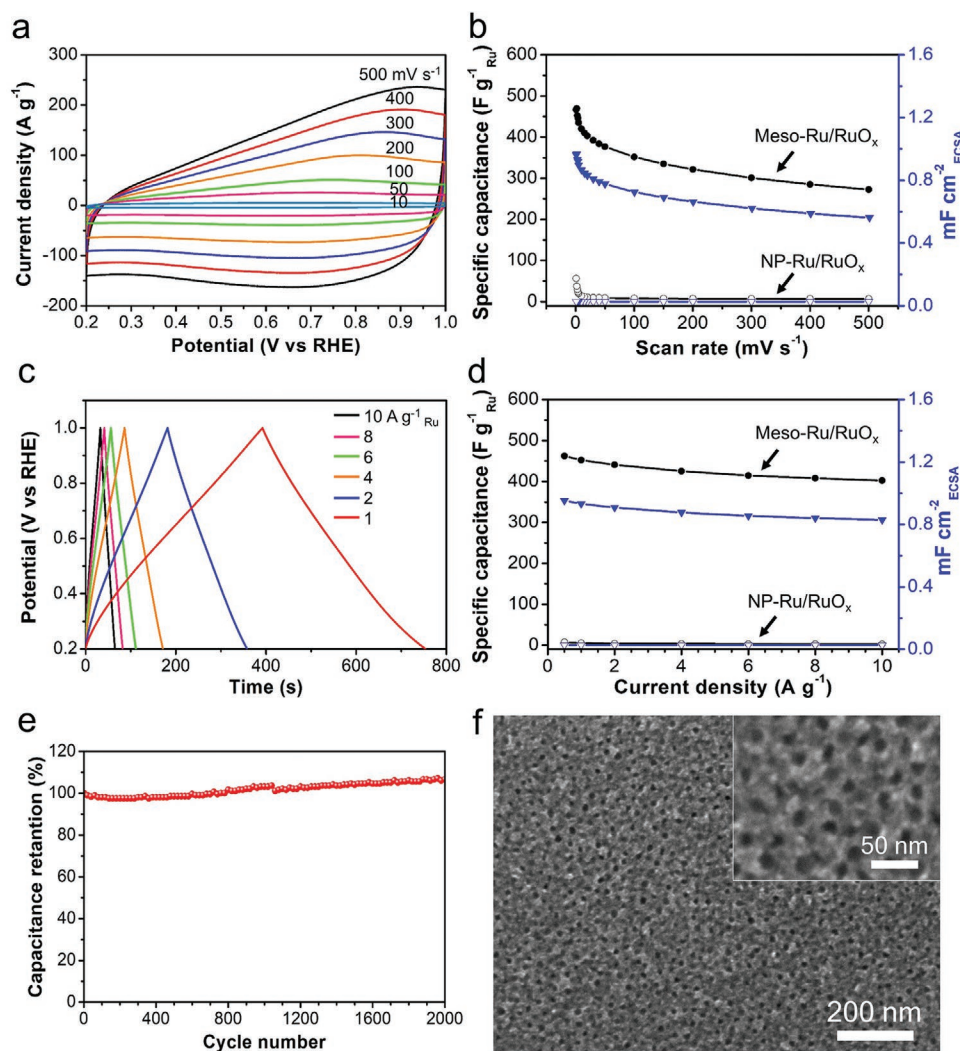


Figure 5. a) CV and c) GCD curves of Meso-Ru/RuO_x obtained at different scan rates and current densities, respectively, in 0.5 M H₂SO₄. b,d) The relationship between specific capacitance and scan rate or current density, respectively. e) Stability test showing capacitance retention over 2000 charge/discharge cycles at a current density of 10 A g⁻¹ Ru. f) Top-surface SEM image of Meso-Ru/RuO_x after stability test. The inset is the magnified SEM image.

is much more challenging. Our electrochemical approach has the capability to overcome this issue and allow the direct synthesis of mesoporous materials for usage in devices. Furthermore, the electrochemical oxidation process described here does not destroy the ultrahigh surface area porous network, enabling superior performance compared to other porous RuO_x materials in supercapacitor applications (Table S1, Supporting Information).

3. Conclusion

Herein, we successfully propose the first example of the electrochemical synthesis of MRF with the help of polymeric micelles as a soft template. In this concept, self-assembled micelles are coordinated by Ru precursors and they move to Au/silicon (Si) substrate to be continuously reduced to get the film. This coordination was studied by UV-vis absorption analysis, and

the micelle formation was also confirmed by TEM observation as well as SANS measurement. The applied potential was selected to obtain the most homogeneous porous structure, and we determined -0.6 V versus Ag/AgCl was the best condition. The as-prepared MRF possesses five times higher ECSA (48.5 m² g⁻¹) than NRF (9.8 m² g⁻¹) owing to the porous structure. The surface of these samples was subsequently modified to RuO_x by electrochemical oxidation process toward supercapacitor electrode. Both XPS and Cu upd stripping measurements prove the formation of this surface oxide layer, while XRD patterns reveal that the crystal structure remains as metallic hcp Ru. Meso-Ru/RuO_x shows by far higher specific capacitance (467 F g⁻¹ Ru, 0.96 mF cm⁻² ECSA) than NP-Ru/RuO_x (28 F g⁻¹ Ru, 0.29 mF cm⁻² ECSA), and this capacitance as well as porous structure are retained well even after 2000 charge/discharge cycles stability test. Our electrochemical route to fabricate mesoporous Ru/RuO_x can allow the design of patterned electrode for the real device by simply modifying the surface

conductivity of substrate. Such flexible design cannot be achieved by conventional method generating powder samples, hence we believe that this simple and well-controlled electrochemical synthesis can cast new insight for other researchers working on Ru oxide-based supercapacitor electrodes.

4. Experimental Section

Chemicals: Poly(ethylene oxide)-*b*-poly(methyl methacrylate) (PEO₍₁₀₅₀₀₎-*b*-PMMA₍₁₈₀₀₀₎) was purchased from Polymer Source. THF and sodium chloride (NaCl) (BioXtra, ≥99.5%) were obtained from Sigma-Aldrich. RuCl₃ was supplied by TCI. H₂SO₄ (98%) was provided by Merck. All the chemicals were used without further purification.

Synthesis of MRFs: MRFs were prepared with an electrochemical soft-templating method using self-assembled block polymer micelles as pore-directing agents and sacrificial templates. Initially, 5 mg of PEO₍₁₀₅₀₀₎-*b*-PMMA₍₁₈₀₀₀₎ was completely dissolved as unimers in 0.5 mL of THF under sonication. 0.5 mL of 4×10^{-2} M aqueous RuCl₃ solution was added to this solution and the volume of the reaction solution was increased to 5 mL by adding distilled water. Since the hydrophobic PMMA segments are not soluble in water, successive additions of aqueous precursor solutions and water induce the micellization of the block copolymer. The Ru precursors interact with the PEO shell of the micelles and decorate its surface (Figure S1, Supporting Information). Electrochemical deposition was performed using a conventional three-electrode system with a Pt counter electrode, Ag/AgCl (3 M NaCl) reference electrode, and Au-coated Si substrate as the working electrode. Upon applying -0.6 V for 1200 s, Ru precursors were codeposited with micelles onto the Au working electrode, where it is reduced continuously to generate a film with a thickness of 100 nm. The deposited area was fixed to 0.18 cm² for all samples. After the completion of electrodeposition, the samples were taken out from the reaction bath and washed in 50 °C THF for 1 min to remove remaining polymers, then rinsed by distilled water (Scheme 1). As a reference sample, NRF was prepared via the same method in the absence of block-polymer micelles. (Note: Spherical micelles can be prepared by Pluronic polymers such as P123, F127, when the concentration is over critical micelle concentration (CMC). However, since these micelles are unstable, it is hard to prepare mesoporous Ru films.)

Characterizations: The morphologies of prepared MRFs were observed by SEM (HITACHI SU-8000) at the accelerating voltage of 5 kV. Furthermore, the internal structure of the pores was investigated with a TEM (JEOL JEM-2100F; 200 kV). HRTEM, HAADF-STEM, and selected area electron diffraction (SAED) patterns were also collected with this instrument. Wide-angle XRD patterns were obtained with a RIGAKU SmartLab 3kW-BU using Cu K α radiation (40 kV 30 mA). For the analyses of surface chemistry, XPS was conducted by Kratos Axis Ultra XPS using a monochromatic Al K α (1486.6 eV) X-ray source. While the mass of deposited Ru can be estimated by the theoretical calculation,

the actual values were also confirmed by inductively coupled plasma optical emission spectroscopy (ICP-OES, HITACHI SPS3520UV-DD). In addition, the interaction between Ru precursors and micelles was examined via UV-vis (JASCO V-7200).

Determination of ECSAs: Traditionally, the ECSAs of platinum group metals can be determined either by carbon monoxide (CO) stripping voltammetry^[44,45] or CV in the hydrogen adsorption/desorption regions.^[46–48] However, the potential of the Ru oxidation peak overlaps with the hydrogen desorption region, so the latter method cannot be used. Moreover, the formation of more than one layer as well as dissolution into metallic Ru may create additional problems. Also, it is not yet well established whether CO adsorbs to the surface of Ru with a 1:1 ratio.^[41,49] Due to these issues, Cu upd stripping is a useful alternative technique to CO stripping because Ru and Cu have similar radii (Ru = 0.134; Cu = 0.128 nm) so Cu atoms deposit on Ru surface with 1:1 ratio.^[41] Hence, all ECSAs reported in this paper use the Cu upd stripping method described in detail next.

All electrochemical experiments were implemented by CHI 660E electrochemical analyzer (CHI Instrument, Inc.) using the same three-electrode system as the case of preparing samples. To make the data easy to compare, the measured potentials were converted to RHE values using the following equation

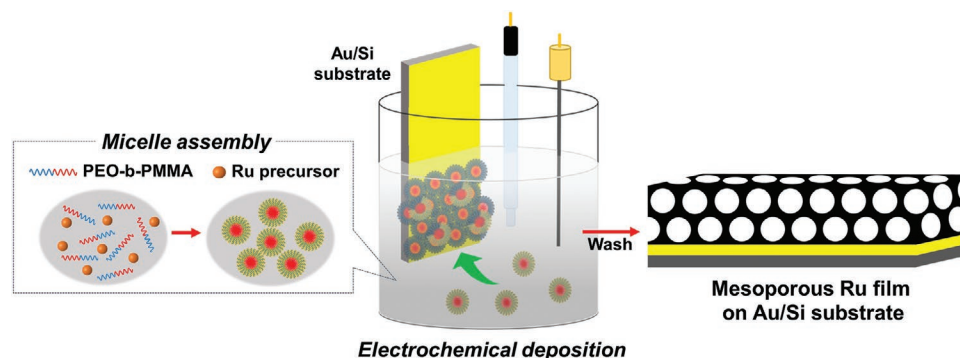
$$E_{\text{RHE}} = E_{\text{Ag/AgCl}} + E_{\text{Ag/AgCl}}^0 + 0.059 \text{ pH} \quad (1)$$

where E_{RHE} is the potential versus RHE, $E_{\text{Ag/AgCl}}$ is the value measured against Ag/AgCl reference electrode, and $E_{\text{Ag/AgCl}}^0$ is the standard potential of this electrode ($E_{\text{Ag/AgCl}}^0 = 0.195$ V vs RHE). Before all measurements, the mesoporous electrodes cleaned electrochemically by cycling the voltage 400 times via CV from 0.05 to 0.8 V at a scan rate of 500 mV s⁻¹ in 0.1 M H₂SO₄. Afterward, one cycle of CV was collected at a slower scan rate (10 mV s⁻¹) to serve as a background for integrating Cu upd peaks. Next, the electrolyte was changed to 0.1 M H₂SO₄ + 2×10^{-2} M CuSO₄, and another CV graph was collected at the same scan rate to investigate the behavior of Cu upd and its stripping. This technique is discussed in more detail in the Supporting Information. Finally, the potential was held at 0.4 V for 300 s to form a monolayer of Cu on the Ru surface, and then LSV was operated from 0.4 to 0.8 V to release this monolayer—completing the so-called Cu upd stripping step. Assuming that the stripping of Cu upd monolayer is a two-electron transfer process ($\text{Cu upd} \rightarrow \text{Cu}^{2+} + 2\text{e}^-$, $420 \mu\text{C cm}^{-2}$),^[50,51] the ECSAs can be calculated with the following equation

$$\text{ECSA} [\text{m}^2 \text{ g}^{-1}] = \frac{Q [\text{A V}]}{\nu [\text{V s}^{-1}] \times Q_0 [\text{C cm}^{-2}] \times m [\text{g}] \times 10000} \quad (2)$$

where Q is the integrated Cu upd stripping peak area, ν is the scan rate (10 mV s⁻¹), Q_0 is the charged density ($420 \mu\text{C cm}^{-2}$), and m is the mass of Ru deposited on the surface.

Performance as a Supercapacitor Electrode: The surface of the as-prepared Ru electrodes was converted to an oxide layer by performing



Scheme 1. Illustration of the electrochemical synthesis of MRF.

500 cycles CV from 0.2 to 1.2 V (vs RHE) at the scan rate of 50 mV s⁻¹ in 0.5 M H₂SO₄. The original micelles determine the resulting pore shapes and pore sizes in the reaction solution. The hydrophobic PMMA unit (i.e., the core of micelles) and hydrophilic PEO unit (i.e., the shell of micelles) generate the pores and pore walls, respectively. Hence, the pore sizes can be controlled by using different molecular weights of PMMA units. Subsequent oxidation does not significantly change these pore shapes and sizes. Their applied times and potentials during the electrochemical oxidation affect only the oxidation degree of the Ru surface.

After the samples were electrochemically oxidized, they were directly used for the performance test toward supercapacitor electrodes. Both CV and GCD measurements were conducted in 0.5 M H₂SO₄ to examine specific capacitance. CVs were collected in the potential range of 0.2–1.0 V versus RHE at various scan rates (e.g., 1, 2, 3, 4, 5, 10, 15, 20, 30, 40, 50, 100, 150, 200, 300, 400, and 500 mV s⁻¹), and the specific capacitances were calculated with the following equation

$$C [F g^{-1}] = \frac{\int IdV [A V]}{2 \times m [g] \times \nu [V s^{-1}] \times \Delta V [V]} \quad (3)$$

where C is the specific capacitance, $\int IdV$ is the integrated area of CV curve, m is the mass of deposited Ru, ν is the scan rate, and the ΔV is the potentials window (1.0 V). GCD properties were investigated by chronopotentiometry (CP) between 0.2 and 1.0 V versus RHE at various current densities (e.g., 0.5, 1, 2, 4, 6, 8, and 10 A g⁻¹), and specific capacitances were calculated again with the following equation

$$C [F g^{-1}] = \frac{I [A] \times \Delta t [s]}{\Delta V [V] \times m [g]} \quad (4)$$

where I is the current density and Δt is the time consumed to complete the discharge process. Additionally, the specific capacitances (mF cm⁻²) were also obtained by replacing m values with S [cm²] (geometric surface area: 0.18 cm²) in Equations (2) and (3).

The stability test was performed by running 2000 charge/discharge cycles at a current density of 10 A g⁻¹ and calculating the specific capacitance for each cycle with Equation (3).

Supporting Information

Supporting Information is available from the Wiley Online Library or from the author.

Acknowledgements

This research was supported by an Australian Government Research Training Program Scholarship and the Australian Research Council Discovery Project (DP190102944). C.S. was supported by Lions Medical Research Foundation (018918), National Health and Medical Research Council – Medical Research Future Fund (1199984), and Fondo Nacional de Desarrollo Científico y Tecnológico (FONDECYT 1170809). This work was also performed in part at the Queensland node of the Australian National Fabrication Facility (ANFF-Q), a company established under the National Collaborative Research Infrastructure Strategy to provide nano and microfabrication facilities for Australia's researchers. The authors acknowledge the facilities, and the scientific and technical assistance, of the Australian Microscopy and Microanalysis Research Facility at the Centre for Microscopy and Microanalysis, The University of Queensland.

Conflict of Interest

The authors declare no conflict of interest.

Keywords

mesoporous films, mesoporous Ru, Ru oxide, supramolecular templates, supercapacitors

Received: April 19, 2020

Revised: June 23, 2020

Published online: August 7, 2020

- [1] B. Jiang, C. Li, Ö. Dag, H. Abe, T. Takei, T. Imai, M. S. A. Hossain, M. T. Islam, K. Wood, J. Henzie, *Nat. Commun.* **2017**, *8*, 15581.
- [2] B. Jiang, C. Li, V. Malgras, M. Imura, S. Tominaka, Y. Yamauchi, *Chem. Sci.* **2016**, *7*, 1575.
- [3] B. Jiang, Y. Guo, J. Kim, A. E. Whitten, K. Wood, K. Kani, A. E. Rowan, J. Henzie, Y. Yamauchi, *J. Am. Chem. Soc.* **2018**, *140*, 12434.
- [4] B. Liu, Y.-F. Zhao, H.-Q. Peng, Z.-Y. Zhang, C.-K. Sit, M.-F. Yuen, T.-R. Zhang, C.-S. Lee, W.-J. Zhang, *Adv. Mater.* **2017**, *29*, 1606521.
- [5] Y. Song, C. Zhu, H. Li, D. Du, Y. Lin, *RSC Adv.* **2015**, *5*, 82617.
- [6] A. S. Nugraha, C. Li, J. Bo, M. Iqbal, S. M. Alshehri, T. Ahamad, V. Malgras, Y. Yamauchi, T. Asahi, *ChemElectroChem* **2017**, *4*, 2571.
- [7] J. K. Shon, S. S. Kong, J. M. Kim, C. H. Ko, M. Jin, Y. Y. Lee, S. H. Hwang, J. A. Yoon, J.-N. Kim, *Chem. Commun.* **2009**, 650.
- [8] H. Wang, H. Y. Jeong, M. Imura, L. Wang, L. Radhakrishnan, N. Fujita, T. Castle, O. Terasaki, Y. Yamauchi, *J. Am. Chem. Soc.* **2011**, *133*, 14526.
- [9] P.-K. Chen, N.-C. Lai, C.-H. Ho, Y.-W. Hu, J.-F. Lee, C.-M. Yang, *Chem. Mater.* **2013**, *25*, 4269.
- [10] G. S. Attard, S. A. Leclerc, S. Maniguet, A. E. Russell, I. Nandhakumar, P. N. Bartlett, *Chem. Mater.* **2001**, *13*, 1444.
- [11] P. N. Bartlett, J. Marwan, *Microporous Mesoporous Mater.* **2003**, *62*, 73.
- [12] Y. Yamauchi, T. Momma, T. Yokoshima, K. Kuroda, T. Osaka, *J. Mater. Chem.* **2005**, *15*, 1987.
- [13] V. Malgras, H. Atae-Esfahani, H. Wang, B. Jiang, C. Li, K. C. W. Wu, J. H. Kim, Y. Yamauchi, *Adv. Mater.* **2016**, *28*, 993.
- [14] G. S. Attard, J. M. Corker, C. G. Göltner, S. Henke, R. H. Templer, *Angew. Chem., Int. Ed. Engl.* **1997**, *36*, 1315.
- [15] W. Sugimoto, S. Makino, R. Mukai, Y. Tatsumi, K. Fukuda, Y. Takasu, Y. Yamauchi, *J. Power Sources* **2012**, *204*, 244.
- [16] L. Wang, Y. Yamauchi, *J. Am. Chem. Soc.* **2009**, *131*, 9152.
- [17] L. Wang, Y. Yamauchi, *J. Am. Chem. Soc.* **2013**, *135*, 16762.
- [18] Y. Yamauchi, A. Tonegawa, M. Komatsu, H. Wang, L. Wang, Y. Nemoto, N. Suzuki, K. Kuroda, *J. Am. Chem. Soc.* **2012**, *134*, 5100.
- [19] M. Iqbal, Y. V. Kaneti, K. Kashimura, M. Yoshino, B. Jiang, C. Li, B. Yulianto, Y. Bando, Y. Sugahara, Y. Yamauchi, *Nanoscale Horiz.* **2019**, *4*, 960.
- [20] C. Li, M. Iqbal, B. Jiang, Z. Wang, J. Kim, A. K. Nanjundan, A. E. Whitten, K. Wood, Y. Yamauchi, *Chem. Sci.* **2019**, *10*, 4054.
- [21] K. Kani, J. Kim, B. Jiang, M. S. A. Hossain, Y. Bando, J. Henzie, Y. Yamauchi, *Nanoscale* **2019**, *11*, 10581.
- [22] C. Li, B. Jiang, Z. Wang, Y. Li, M. S. A. Hossain, J. H. Kim, T. Takei, J. Henzie, Ö. Dag, Y. Bando, Y. Yamauchi, *Angew. Chem., Int. Ed.* **2016**, *55*, 12746.
- [23] B. Jiang, K. Kani, M. Iqbal, H. Abe, T. Kimura, M. S. A. Hossain, O. Anjaneyulu, J. Henzie, Y. Yamauchi, *Chem. Mater.* **2018**, *30*, 428.
- [24] M. Iqbal, Y. Kim, C. Li, B. Jiang, T. Takei, J. Lin, B. Yulianto, Y. Bando, J. Henzie, Y. Yamauchi, *ACS Appl. Mater. Interfaces* **2019**, *11*, 36544.
- [25] A. S. Nugraha, V. Malgras, M. Iqbal, B. Jiang, C. Li, Y. Bando, A. Alshehri, J. Kim, Y. Yamauchi, T. Asahi, *ACS Appl. Mater. Interfaces* **2018**, *10*, 23783.

- [26] A. González, E. Goikolea, J. A. Barrena, R. Mysyk, *Renewable Sustainable Energy Rev.* **2016**, 58, 1189.
- [27] W. Sugimoto, H. Iwata, K. Yokoshima, Y. Murakami, Y. Takasu, *J. Phys. Chem. B* **2005**, 109, 7330.
- [28] J. Zheng, P. Cygan, T. Jow, *J. Electrochem. Soc.* **1995**, 142, 2699.
- [29] R. Fu, Z. Ma, J. P. Zheng, *J. Phys. Chem. B* **2002**, 106, 3592.
- [30] J. Zheng, T. Jow, *J. Electrochem. Soc.* **1995**, 142, L6.
- [31] K.-H. Chang, C.-C. Hu, *Electrochem. Solid-State Lett.* **2004**, 7, A466.
- [32] K.-H. Chang, C.-C. Hu, C.-Y. Chou, *Chem. Mater.* **2007**, 19, 2112.
- [33] J. W. Long, K. E. Swider, C. I. Merzbacher, D. R. Rolison, *Langmuir* **1999**, 15, 780.
- [34] A. Sokolova, A. E. Whitten, L. de Campo, J. Christoforidis, A. Eltobaji, J. Barnes, F. Darmann, A. Berry, *J. Appl. Crystallogr.* **2019**, 52, 1.
- [35] S. R. Kline, *J. Appl. Crystallogr.* **2006**, 39, 895.
- [36] P. V. Konarev, V. V. Volkov, A. V. Sokolova, M. H. Koch, D. I. Svergun, *J. Appl. Crystallogr.* **2003**, 36, 1277.
- [37] H. H. Cady, R. E. Connick, *J. Am. Chem. Soc.* **1958**, 80, 2646.
- [38] R. E. Connick, D. A. Fine, *J. Am. Chem. Soc.* **1960**, 82, 4187.
- [39] Ö. Çelik, Ö. Dag, *Angew. Chem., Int. Ed.* **2001**, 40, 3799.
- [40] S. Hadz, H. Angerstein-Kozłowska, M. Vuković, B. Conway, *J. Electrochem. Soc.* **1978**, 125, 1471.
- [41] C. L. Green, A. Kucernak, *J. Phys. Chem. B* **2002**, 106, 1036.
- [42] D. J. Morgan, *Surf. Interface Anal.* **2015**, 47, 1072.
- [43] H. Lim, J. Kim, K. Kani, M. K. Masud, H. Park, M. Kim, S. M. Alsheri, T. Ahamad, N. Alhokbany, J. Na, V. Malgras, Y. Bando, Y. Yamauchi, *Small* **2020**, 16, 1902934.
- [44] P. Waszczuk, J. Solla-Gullon, H.-S. Kim, Y. Tong, V. Montiel, A. Aldaz, A. Wieckowski, *J. Catal.* **2001**, 203, 1.
- [45] J. Durst, C. Simon, F. Hasché, H. A. Gasteiger, *J. Electrochem. Soc.* **2015**, 162, F190.
- [46] B. L. Abrams, P. C. Vesborg, J. L. Bonde, T. F. Jaramillo, I. Chorkendorff, *J. Electrochem. Soc.* **2009**, 156, B273.
- [47] B. T. X. Lam, M. Chiku, E. Higuchi, H. Inoue, *Adv. Nanopart.* **2016**, 5, 60.
- [48] M. Łukaszewski, H. Siwek, A. Czerwiński, *Electrochim. Acta* **2007**, 52, 4560.
- [49] K. Kinoshita, *J. Electroanal. Chem. Interfacial Electrochem.* **1977**, 78, 313.
- [50] J. Ohyama, T. Sato, Y. Yamamoto, S. Arai, A. Satsuma, *J. Am. Chem. Soc.* **2013**, 135, 8016.
- [51] J. M. Sieben, M. M. E. Duarte, C. E. Mayer, *J. Appl. Electrochem.* **2008**, 38, 483.